

Article

Island-Type Hybrid Catalysts Applied for Anion Exchange Membrane Water Electrolysis

Hsueh-Yu Chen ¹, Guan-Cheng Chen ¹, Kuo-Wei Liao ¹ , Wen-Hui Wei ¹, Hsin-Chih Huang ^{2,*} and Chen-Hao Wang ^{1,3,*} 

¹ Department of Materials Science and Engineering, National Taiwan University of Science and Technology, Taipei 106335, Taiwan; codo1270@gmail.com (H.-Y.C.); D10104019@mail.ntust.edu.tw (G.-C.C.); wales11720@gmail.com (K.-W.L.); wenhui0113@gmail.com (W.-H.W.)

² Global Development Engineering Program, National Taiwan University of Science and Technology, Taipei 106335, Taiwan

³ Center of Automation and Control, National Taiwan University of Science and Technology, Taipei 106335, Taiwan

* Correspondence: hchuang@mail.ntust.edu.tw (H.-C.H.); chwang@mail.ntust.edu.tw (C.-H.W.)

Abstract: A rapid, productive, and efficient process was invented to produce hybrid catalysts for transition metal oxide water electrolysis. The microwave-assisted hydrothermal method was applied to synthesize transition metal oxide catalysts by controlling the amount of cobalt and iron. This work solves the cracking problem for the catalytic layer during the water electrolysis. It uses Fe₂O₃ as the support and covers a catalytic layer outside it and a nanoscale gap between each catalyst, which can help to remove the gas and fill up the water. The unique structure of the catalysts can prevent them from accumulating gas and increasing their efficiency for long-term water electrolysis. By using unique catalysts in the water electrolyzer, the current density reaches higher than 200 mA cm⁻² at 2.0 V and does not show a significant decay even after 200 h.

Keywords: oxygen evolution reaction; water electrolysis; island-type; transition metal oxide



Citation: Chen, H.-Y.; Chen, G.-C.; Liao, K.-W.; Wei, W.-H.; Huang, H.-C.; Wang, C.-H. Island-Type Hybrid Catalysts Applied for Anion Exchange Membrane Water Electrolysis. *Catalysts* **2022**, *12*, 102. <https://doi.org/10.3390/catal12010102>

Academic Editors: Valeria La Parola and David Sebastián

Received: 10 November 2021

Accepted: 11 January 2022

Published: 17 January 2022

Publisher's Note: MDPI stays neutral with regard to jurisdictional claims in published maps and institutional affiliations.



Copyright: © 2022 by the authors. Licensee MDPI, Basel, Switzerland. This article is an open access article distributed under the terms and conditions of the Creative Commons Attribution (CC BY) license (<https://creativecommons.org/licenses/by/4.0/>).

1. Introduction

Water electrolysis is one of the crucial ways to produce high purity of hydrogen and oxygen. For the traditional water electrolysis, the catalyst of the anode is IrO₂, and the cathode is Pt/C [1–3]. Due to the high price of precious metal catalysts, several studies have been used non-precious metal catalysts to replace precious metal catalysts for oxygen evolution reaction (OER) [4–6]. Some researchers have indicated that the spinel structure of transition metal oxides like Fe, Co, and Ni, can effectively reduce the overpotential of the reaction, especially in alkaline media [7,8]. Compared to carbon-based materials, non-precious metal oxides are more stable under the harsh conditions of water electrolysis. Considering the characteristic of different types of the spinel structure, the AB₂X₄ (A and B = metals, X = chalcogen element) spinel compound is a promising functional material with controllable active sites [9]. Besides its advantages of low cost, acceptable content, low toxicity, and multivalent states, some spinel structures also present a special Jann-Taylor effect. In these classic spinel structures, X²⁻ are closed packed, A²⁺ and B³⁺ occupy the most tetrahedral and octahedral sites [10,11]. Different arrangements of the ions in the spinel structure and different phases exploring will affect the spinel electronic structure and chemical properties [12].

Most transition metal oxides are magnetic, efficiently aggregating together after the synthesis. The aggregation of the catalysts may decrease the surface area, even seal the gas produced by the reaction and further occupy the active site of the catalysts. Moreover, the encased gas cannot be exhausted from the catalytic layer. In that case, it will crack the catalytic layer and increase the reaction's resistance, resulting in diminishing the transfer

efficiency. Some researchers have mentioned that controlling the structure of the catalysts can improve this phenomenon. Yang, et al. demonstrated the unique structure with a thin shell with large pores. The pores come from the phase transformation and can help release oxygen from the reaction. These pores can even help the electrolyte infiltrate the catalysts for further continued processes [13]. Zhang et al. expounded a multiporous core-shell structure of cobalt by electrodeposition method. They deposited thin layered $\text{Co}(\text{OH})_2$ on the CoS_2 nanofiber using cycle voltammetry (CV) and did anodizing to make $\text{Co}(\text{OH})_2$ become CoO_x catalysts. This method can form the layer structure covered fiber catalysts. The unique morphology and small size substantially increase the surface area of the catalysts, leading to the high efficiency of the electrotransfer and electrochemical activity [14].

Some researches indicate that the transition metal oxide can improve the catalytic activity for the OER [4–6,10,11]. Some researchers also specify the benefits of the structural design of the catalysts [12–14]. This work chooses the facile heating method of microwave and uses the active cobalt compounds to cover iron oxide. By adjusting the ratio of the precursors, we have successfully fabricated the unique island-type porous structure, which increases the efficiency of gas removal and stability.

2. Results and Discussion

The activity of different ratios of iron and cobalt for the OER was carried out by electrochemical test in 1.0 M KOH solution. Figure 1a shows the results of LSV curves. The pristine Fe_2O_3 shows the highest onset potential of 1.68 V. However, the onset potential is reduced by adding CoCl_2 to the catalyst, which means that the cobalt compound in these catalysts plays a significant role to enhance the activity of the OER. 1.54 V is the lowest onset potential for the sample of $\text{Co-Fe}_2\text{O}_3$ (60:3) compared to other samples. Figure 1b presents the Tafel slope of the catalysts. The lower slope signifies less energy consumption during the OER reaction. The pristine Fe_2O_3 and without Fe_2O_3 samples show the slope of 185 mV dec^{-1} and 71 mV dec^{-1} , respectively. The ratio of $\text{Co-Fe}_2\text{O}_3$ (60:3) shows the lowest slope of 29 mV dec^{-1} compared to other samples. The slope for other ratios is 34 mV dec^{-1} for $\text{Co-Fe}_2\text{O}_3$ (20:3), 36 mV dec^{-1} for $\text{Co-Fe}_2\text{O}_3$ (40:3), and 32 mV dec^{-1} for $\text{Co-Fe}_2\text{O}_3$ (80:3), indicating that the hybrid catalysts can efficiently decrease the energy consumption of the OER. In the alkaline media of the OER, the value of the Tafel slope can determine which one of the 4 electron transfer steps in OER is the rate-determining step (RDS) [15]. If the RDS is in the first electron transfer, the Tafel slope is near 120 mV dec^{-1} . Suppose the RDS is in the chemical reaction; after a one-electron transfer reaction, the Tafel slope is near 60 mV dec^{-1} . If the RDS is in the third electron transfer step, the Tafel slope is near 30 mV dec^{-1} . The smaller Tafel slope means the RDS is near the electron transfer's end step, potential catalysts [16–18]. The RDS of hybrid catalysts in this work should be near to a favorable third electron transfer step [19]. Additionally, the $\text{Co-Fe}_2\text{O}_3$ (60:3) presents the highest activity among other ratios owing to its unique structure and high surface area.

Figure 2 shows the SEM images for different compositions of the catalysts. Figure 2a displays the morphology of $\text{Co-Fe}_2\text{O}_3$ (20:3); it presents some small spheres stuck together. Figure 2b shows the morphology of $\text{Co-Fe}_2\text{O}_3$ (40:3); it gives more prominent spheres but still aggregates a lot. Figure 2c depicts the morphology of $\text{Co-Fe}_2\text{O}_3$ (60:3); it presents significant spheres close together. Figure 2d shows the morphology of $\text{Co-Fe}_2\text{O}_3$ (80:3); it offers some pieces stacked together. From controlling the composition of the catalysts, the structure keeps growing, and $\text{Co-Fe}_2\text{O}_3$ (60:3) shows the most proper structure without aggregation, resulting in the island-type catalyst. The function of iron oxide plays the raw support to prevent the magnetic Co-based catalysts from aggregating together.

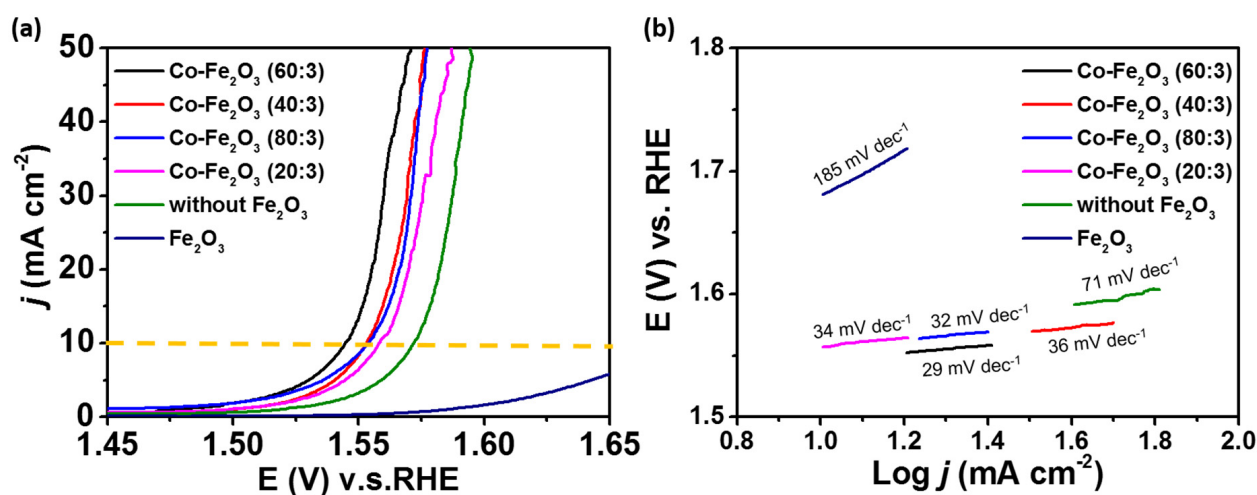


Figure 1. The activity of OER for different ratios between iron and cobalt precursors with *iR*-compensated. (a) LSV curves. (b) Tafel slopes.

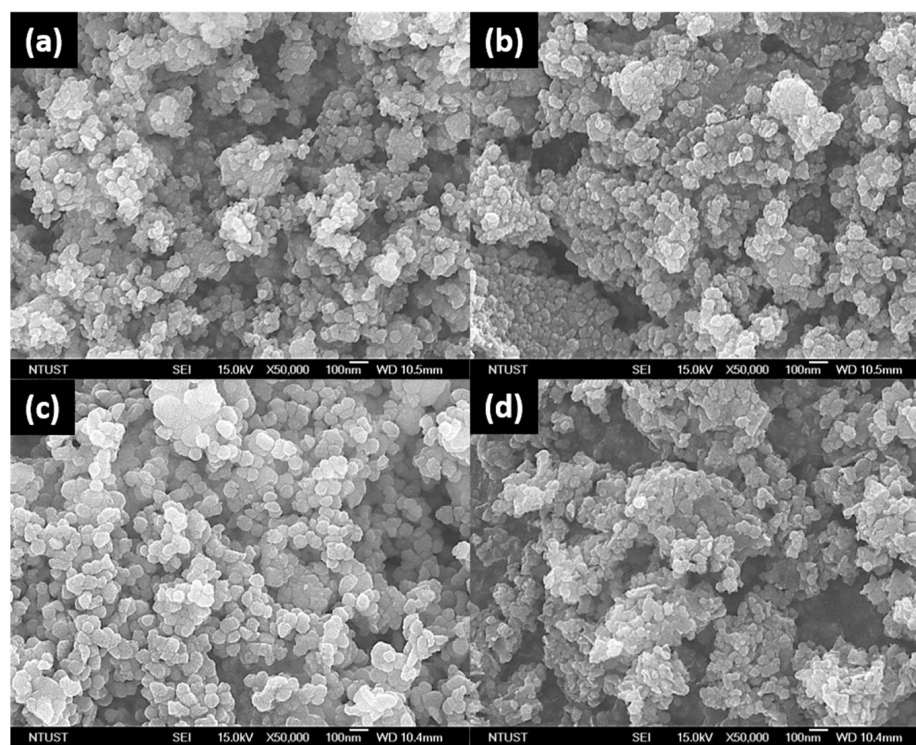


Figure 2. The SEM images for different ratios between iron and cobalt precursors. (a) Co-Fe₂O₃ (20:3), (b) Co-Fe₂O₃ (40:3), (c) Co-Fe₂O₃ (60:3), and (d) Co-Fe₂O₃ (80:3).

Figure 3 shows the XRD patterns for different samples. The amount of CoCl₂ increases from 200 to 800 mg, and the product of the catalysts turn from Co₃O₄ to Co(OH)₂. Due to the acidic nature of the CoCl₂ solution, when increasing the amount of CoCl₂, it needs more NaOH to let the solution become alkaline. Controlling the pH value can make the size of the cobalt compound consistent [20]. As a higher concentration of OH⁻ in the solution, the catalysts tend to be Co(OH)₂.

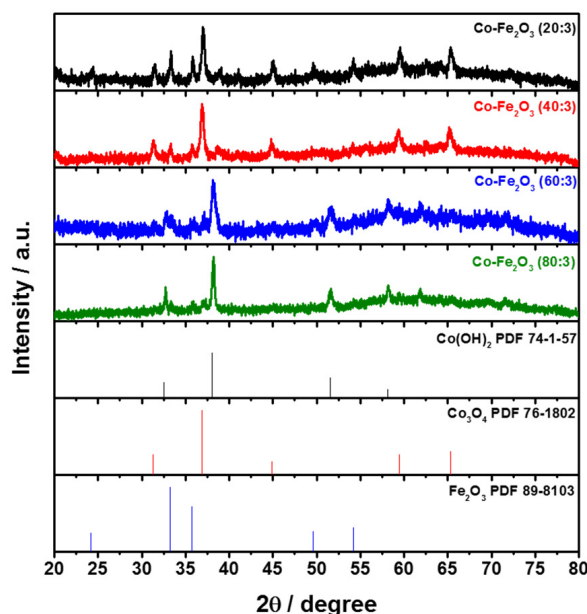


Figure 3. XRD patterns for different ratios between iron and cobalt precursors.

To further realize the relationship between the major compounds in the catalysts, Figure S1 displays the XPS of Fe 2p spectra, and Figure 4 shows the XPS of Co 2p spectra. In Figure S1., the peaks around 711.2 eV and 709.2 eV represent the existence of Fe³⁺ and Fe²⁺ [21]. They also show a Co LMM at around 713 eV to decrease the overlapping influence. After integrating the area of the peaks, the percentage between Fe²⁺ and Fe³⁺ for the catalysts is shown in Table S1. It indicates that changing the amount of the precursor for the cobalt cannot be affected the valence state of the iron support. The ratio between Fe²⁺ and Fe³⁺ is all around 1:2. In Figure 4, the peaks around 779.4 eV and 780.6 eV represent the existence of Co³⁺ and Co²⁺ [22]. From integrating the area of the peaks, Table 1 shows that when increasing the amount of cobalt precursor, the amount of Co²⁺ also increases. This result coincides with the results of the XRD. The ratio between Co³⁺ and Co²⁺ is changed from 7:3 to 4:6. Several studies have shown that the Co³⁺ in spinal structure plays a key role in the OER activity [23,24]. Additionally, it indicates that the Co(OH)₂ is also beneficial to the OER activity because of its superior adsorption ability to the intermediates of *OOH from the strong M–OH bonding [25,26]. An appropriate amount of Co³⁺ and Co²⁺ is evidence for the great activity improvement for the Co-Fe₂O₃ (60:3) catalyst towards OER.

Figure 5 shows the BET result of different ratios of the catalysts. From the International Union of Pure and Applied Chemistry chemical nomenclature (IUPAC) classification, the adsorption and desorption curves in Figure 5 are classified as type III isotherm. Type III means the force between the gas and the catalysts is smaller than the force between the gas and the gas [27]. The type of the pores may be the other reason why the island-type hybrid catalysts can have outstanding stability because of the quick removal of the produced gas from the surface of the electrode. The catalysts' structure and activity sites can be remained by these properties. The surface areas for Co-Fe₂O₃ (40:3), Co-Fe₂O₃ (60:3), Co-Fe₂O₃ (80:3), and without the Fe₂O₃ support are 53.87 m² g⁻¹, 73.98 m² g⁻¹, 43.17 m² g⁻¹, and 18.62 m² g⁻¹, respectively. The catalyst of Co-Fe₂O₃ (60:3) performs the highest surface area among other samples, which means the catalysts have more active sites for the OER. The hybrid catalysts' electrochemical surface area (ECSA) is also calculated by the CV method and shown in Figure S2. The ECSA of Co-Fe₂O₃ (40:3), Co-Fe₂O₃ (60:3), and Co-Fe₂O₃ (80:3) are 3.3 m² g⁻¹, 2.3 m² g⁻¹, and 2.1 m² g⁻¹, respectively. The tendency of the surface area and the electrochemical surface area is similar, which further proves that the increase of the active site is related to the surface area of the catalysts.

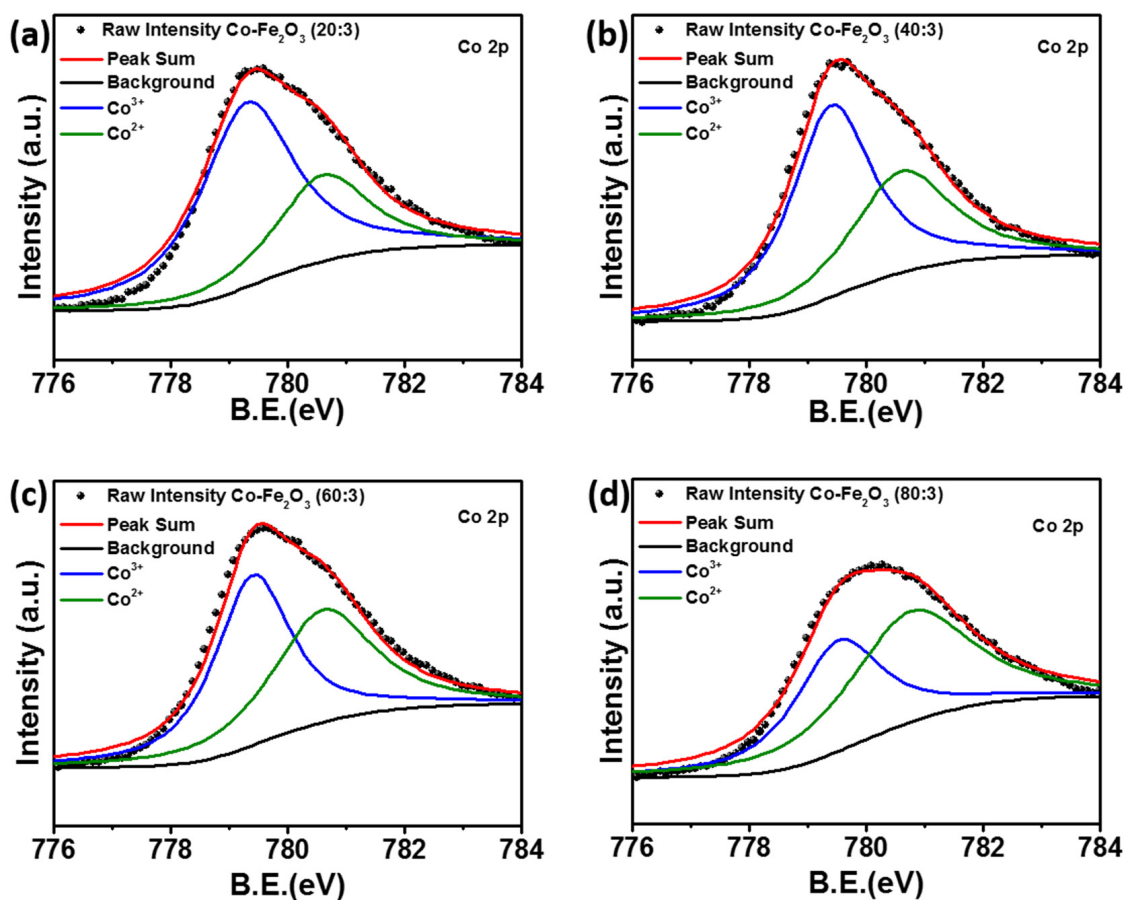


Figure 4. The XPS of Co 2p spectra for (a) Co-Fe₂O₃ (20:3), (b) Co-Fe₂O₃ (40:3), (c) Co-Fe₂O₃ (60:3), and (d) Co-Fe₂O₃ (80:3).

Table 1. The XPS of integrated value for Co³⁺ and Co²⁺.

Sample	Co ³⁺ (%)	Co ²⁺ (%)
Co-Fe ₂ O ₃ (20:3)	68.59	31.41
Co-Fe ₂ O ₃ (40:3)	61.01	38.99
Co-Fe ₂ O ₃ (60:3)	53.50	46.50
Co-Fe ₂ O ₃ (80:3)	42.37	57.63

Figure 6 shows the TEM of the island-type hybrid catalysts for the optimized one of Co-Fe₂O₃ (60:3), in which Figure 6a shows the clear porous structure of the catalysts and Figure 6b shows the HRTEM of the catalysts. The edge of the catalysts indicates the d-spacing of 0.275 nm, corresponding to the (100) plane of cobalt hydroxide. The center of the catalysts shows the d-spacing of 0.251 nm, corresponding to the (110) plane of the iron oxide. Figure 6c–e shows the EDS mapping of the catalysts to distinguish the distribution of the elements. As observed from the EDS mapping, the distribution of Co and O in the sample area is almost identical. However, the signal of Fe is relatively weak compared to the other elements. The weak signal of the iron is due to the cobalt hydroxide covering the surface of the iron oxide, which further proves the existence of the island-type hybrid structure.

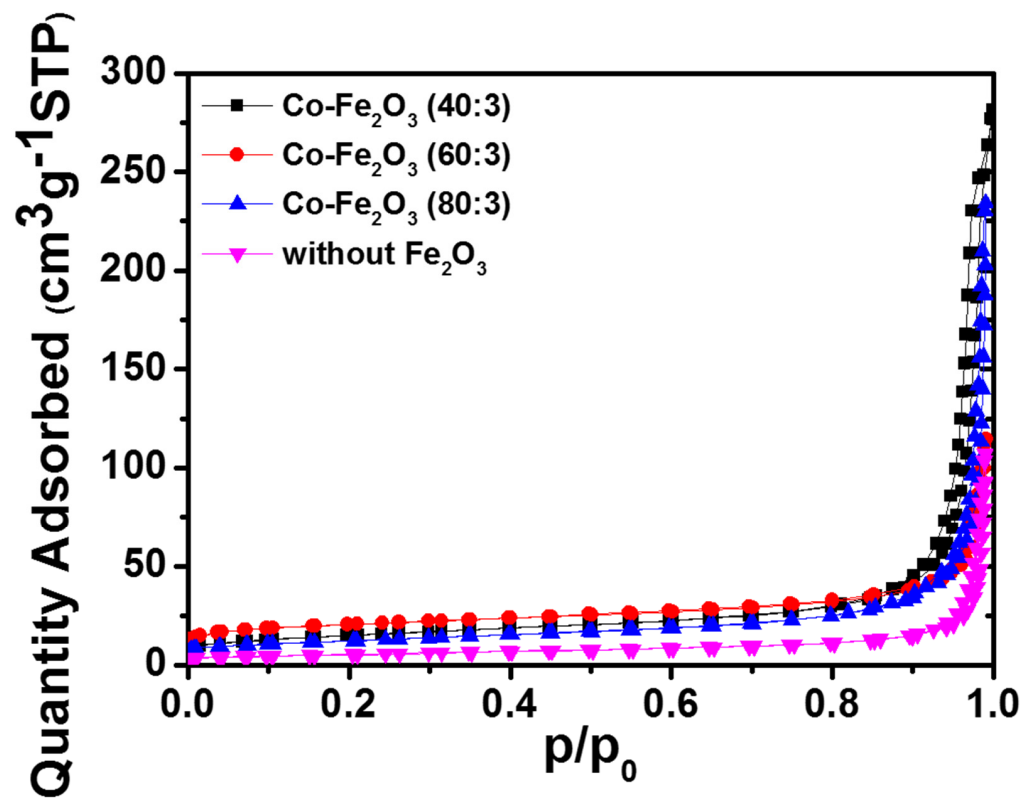


Figure 5. The nitrogen adsorption/desorption curves for different iron and cobalt precursors ratios.

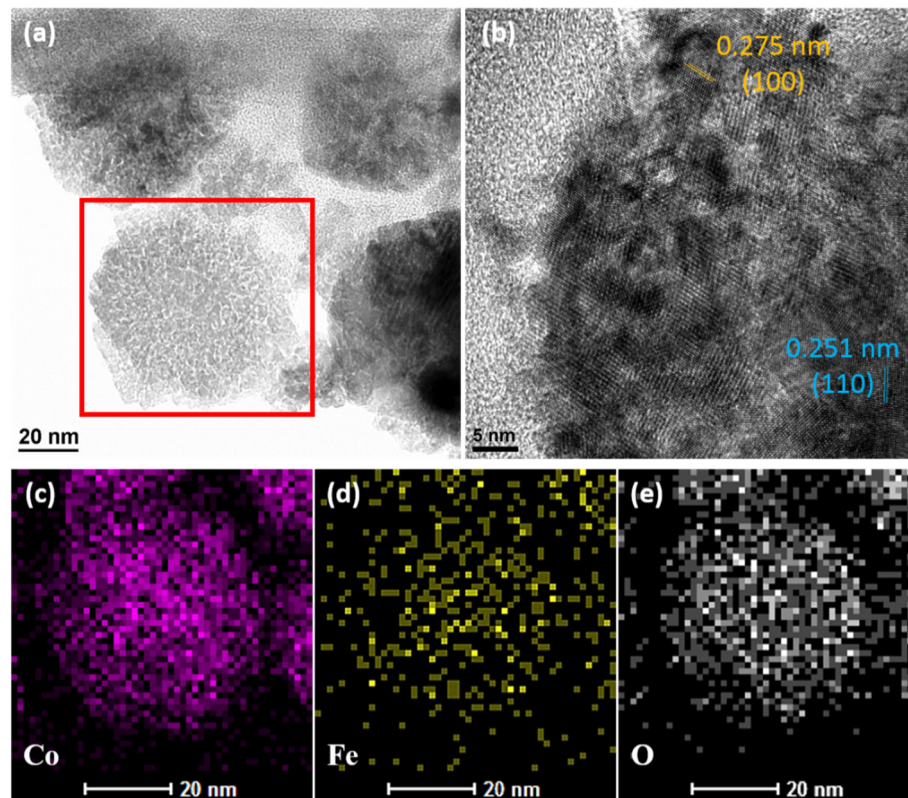


Figure 6. The TEM for $\text{Co-Fe}_2\text{O}_3$ (60:3). (a) The morphology of island-type hybrid catalysts. (b) The HRTEM of island-type hybrid catalysts. The EDS mapping for (c) cobalt, (d) iron, (e) oxygen.

To know the potential of the catalysts for the industrial application, a water electrolyzer test was performed for long-term operation, as shown in Figure 7. Figure 7a shows the stability done by the constant potential method at 2.0 V for 200 h. At the beginning of the trial, the average current density is around 200 mA cm^{-2} for the early 100 h. After the operation of 100 h, it shows a little bit of decay for the current density. The final current density after 200 h is around 180 mA cm^{-2} , which remains 90% of the current density. Figure 7b shows the LSV curves before and after the stability test to understand the activity of the catalysts. It presents that the onset potential of the catalysts is almost similar before and after the stability test. These results indicate that the island-type hybrid catalysts exhibit high activity and outstanding stability. Table 2 shows the onset potentials of OER and the stability tests in alkaline media for the transition metal oxide catalysts, which have been published in recent years. The outstanding stability of the present material under high current density compared to other previously published papers makes the great potential of industrial application for water electrolysis.

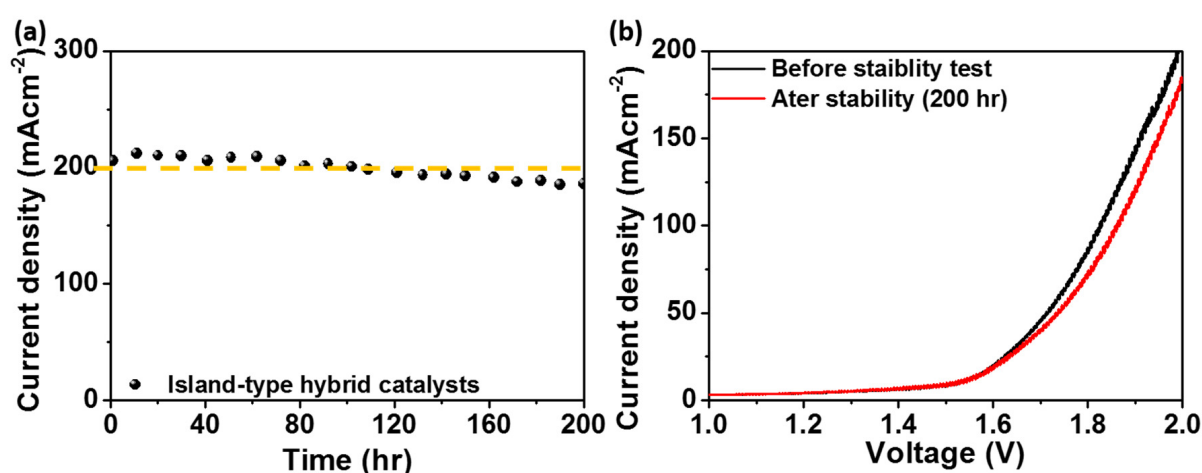


Figure 7. The stability test of the full-water electrolysis. (a) At 2.0 V for 200 h and (b) the LSV curves before and after the stability test.

Table 2. Catalytic properties of transition metal oxide electrocatalysts in alkaline media (1.0 M KOH).

Catalysts	OER Potential @10 mA/cm ²	Water Electrolysis Stability E@j (mA/cm ²)	Operation Time (hour)	Temp. (°C)	Reference
		Half-cell			
$\gamma\text{-Fe}_2\text{O}_3\text{@FeS}_2\text{@C}$	1.50 V	1.50 V@10	10	RT	[21]
$\text{Co}_3\text{O}_4/\text{Fe}_2\text{O}_3$	1.54 V	1.54 V@10	20	RT	[28]
$\text{Ni-Fe}_2\text{O}_3$	1.51 V	1.51 V@10	10	RT	[29]
$\text{Fe}_2\text{O}_3/\text{CoOx-Ar}/\text{H}_2$	1.54 V	1.55 V@10	16	RT	[30]
$\text{M-Co}_3\text{O}_4/\text{NPC}$	1.53 V	1.53 V@10	10	RT	[31]
$\text{Co}_3\text{O}_4/\text{CoMoO}_4/\text{N}$	1.50 V	1.50 V@10	10	RT	[32]
		Full-cell			
$\text{Co-Fe}_2\text{O}_3$ (60:3)	1.54 V	2.0 V@200	200	RT	This work
NiFe nanofoam	-	2.1 V@200	160	60 °C	[33]
$\text{Fe}_x\text{Ni}_y\text{OOH-20F}$	1.48 V	1.7 V@200	160	80 °C	[34]
Co-Fe-MOF74	1.49 V	1.51 V@20	50	RT	[35]
$\text{Fe}_{0.5}\text{Co}_{0.5}\text{@NC/NCNS-800}$	1.50 V	1.50 V@10	30	RT	[36]

The island-type hybrid catalyst was fabricated with the support of Fe_2O_3 and the synergistic effect of Co_3O_4 and Co(OH)_2 . The suitable ratio between the precursors makes the catalyst has abundant active sites and high surface area and form the appropriate structure that is easy for the gas exhausting. These features make that the catalyst has high activity and long-term stability.

3. Experimental

3.1. Preparation of Fe₂O₃

0.75 mL of 0.5 M oxalic acid (C₂H₂O₄) and 1 mL of 1 M NaOH were added into 2 mL of FeCl₃ and deionized water mixture. The solution was mixed uniformly through ultrasonic stirring for 10 min and subjected to microwave-assisted hydrothermal treatment by heating the mixed solution in a Teflon-lined microwave digestion vessel at 160 °C for 30 min. The solution was filtered and washed with deionized water for at least 1 L and placed in a freeze drier overnight to obtain Fe₂O₃.

3.2. Preparation of Island-Type Hybrid Catalysts

The process was the preparation of Fe₂O₃, 0.75 mL of 0.5 M oxalic acid (C₂H₂O₄), and 1 mL of 1 M NaOH were added into 2 mL of Fe₂O₃, CoCl₂, and deionized water mixture; the mass ratios of Fe₂O₃:CoCl₂ was set to be 3:20, 3:40, 3:60, and 3:80. After the ultrasonic stirring for 10 min, 1 M of NaOH solution was added to control the pH value at ten and then transferred the solution into a Teflon-lined microwave digestion vessel. The vessel was treated at 160 °C for 30 min by microwave-assisted hydrothermal method. The solution was then filtered, washed with deionized water, and placed in a freeze drier overnight to obtain the island-type hybrid catalysts.

3.3. Electrochemical Measurement

The electrochemical performance test was conducted on a Solartron 1280B potentiostat (Solartron Group Co., Farnborough, UK) via a three-electrode system in the electrolyte of 1.0 M KOH. The Pt foil and the reversible hydrogen electrode (RHE) were used as the counter and reference electrodes, respectively. A rotating gold disk electrode (RDE, PINE AFE3T050AU) (Pine Research Co., Durham, NC, USA) was used as the working electrode. Thirty-five milligrams of a specific catalyst was mixed with 5 mL of n-propanol, 5 mL of deionized water, and 0.1 mL of 5 wt% Nafion solution to prepare the catalyst ink. The 11.2 µL of the catalyst ink was loaded on the Au disk and then dried in the air. Linear sweep voltammetry (LSV) with the scan rate of 10 mV s⁻¹ was applied to determine the OER activity. The catalyst loading amount was controlled to 0.2 mg cm⁻². The 85% *iR* compensation was applied to the electrochemical measurement [37,38].

3.4. Material Characterization

A transmission electron microscope (TEM) with an acceleration voltage of 200 kV was performed on an FEI TecnaiTM G2 F-20 S-TWIN (FEI Co., Northeast Dawson Creek Dr Hillsboro, OR, USA). X-ray diffraction (XRD) was performed on a Bruker D2 Phaser (Bruker Corp., Billerica, MA, USA) with Cu K α radiation. X-ray photoelectron spectroscopy (XPS) was carried out using a Thermo K-alpha XPS spectrometer (Thermo Fisher Scientific Inc., Waltham, MA, USA) with an Al K α source. The surface area and porosity analyzer were analyzed on a Micrometry Tristar 3000 (Micromeritics Co., Norcross, GA, USA).

3.5. Full Water Electrolysis Test with Anion Exchange Membrane

For the water electrolysis test, the area membrane-electrode-assembly (MEA) was 2.25 cm². A Fumapem FAA-3 membrane (OH⁻, FuMA-Tech GmbH) (Fumatech Co., Bietigheim-Bissingen, Germany) was sandwiched by anode and cathode electrodes. The electrodes were prepared by the hand painting method by loading the as-prepared catalyst and Pt/C catalyst on carbon cloth for the anode and cathode. The catalyst loading was 1.5 and 0.25 mg cm⁻² for anode and cathode electrodes. The catalyst ink was prepared by dispersing in Fumion FAA-3 solution and then dried in the oven for 1 h. The mass ratio of the catalyst to dry FAA-3 was controlled at 3:1. The electrolyte for the test was 1 M KOH, and the flow rate was 100 mL min⁻¹. The stability and LSV tests were done by employing the four-electrode method.

4. Conclusions

The facile process of the microwave-assisted hydrothermal method produces a low cost, high activity, and outstanding stability of the island-type hybrid catalyst for water electrolysis. The island-type structure synthesized by a specific ratio between cobalt precursor and Fe₂O₃ has a high surface area and ECSA compared to other samples. The support of Fe₂O₃ well disperses the active site and contributes to the success of the island-type structure as the center. The active site comes from the Co³⁺ of the Co₃O₄ and Co²⁺ of the Co(OH)₂. Combining these two compounds results in the high activity of the catalysts. The unique porous structure is easier to remove the gas produced during the water electrolysis, thus has outstanding stability. The full cell water electrolysis operated for 200 h at 2.0 V, and the current density reaches higher than 200 mA cm⁻². The onset potential shows no significant decays after the full cell water electrolysis operation. The current density remains 90%, which can be considered the potential candidate for industrial application.

Supplementary Materials: The following supporting information can be downloaded at: <https://www.mdpi.com/article/10.3390/catal12010102/s1>. Figure S1: The XPS of Fe 2p spectra for (a) Co-Fe₂O₃ (20:3), (b) Co-Fe₂O₃ (40:3), (c) Co-Fe₂O₃ (60:3), (d) Co-Fe₂O₃ (80:3); Figure S2: The CV method near the non-faradic potential window: (a) Co-Fe₂O₃ (40:3), (b) Co-Fe₂O₃ (60:3), (c) Co-Fe₂O₃ (80:3), and (d) the scan rates vs. the non-faradic currents for all samples.; Table S1: The XPS of integrated value for Fe³⁺, Fe²⁺, and Co LMM.

Author Contributions: Conceptualization, H.-Y.C., G.-C.C. and C.-H.W.; methodology, H.-Y.C. and G.-C.C.; software, H.-Y.C. and G.-C.C.; validation, H.-Y.C.; formal analysis, H.-Y.C. and G.-C.C.; investigation, K.-W.L. and W.-H.W.; resources, C.-H.W.; data curation, H.-Y.C.; writing—original draft preparation, H.-Y.C.; writing—review and editing, H.-C.H. and C.-H.W.; supervision, H.-C.H. and C.-H.W.; project administration, C.-H.W. All authors have read and agreed to the published version of the manuscript.

Funding: This research was funded by the Ministry of Science and Technology of Taiwan (MOST 110-3116-F-011-004) and the National Taiwan University of Science and Technology-Tokyo Institute of Technology Joint Research Program.

Data Availability Statement: The data presented in this study are available in supplementary material.

Acknowledgments: For X-ray photoelectron spectroscopy (XPS), the authors acknowledge the National Synchrotron Radiation Research Center (Beamline 24A), Hsinchu, Taiwan, for X-ray photoelectron spectroscopy (XPS).

Conflicts of Interest: The authors declare no conflict of interest.

References

1. Lee, Y.; Suntivich, J.; May, K.J.; Perry, E.E.; Shao-Horn, Y. Synthesis and Activities of Rutile IrO₂ and RuO₂ Nanoparticles for Oxygen Evolution in Acid and Alkaline Solutions. *J. Phys. Chem. Lett.* **2012**, *3*, 399–404. [[CrossRef](#)]
2. Reier, T.; Oezaslan, M.; Strasser, P. Electrocatalytic Oxygen Evolution Reaction (OER) on Ru, Ir, and Pt Catalysts: A Comparative Study of Nanoparticles and Bulk Materials. *ACS Catal.* **2012**, *2*, 1765–1772. [[CrossRef](#)]
3. Sardar, K.; Petrucco, E.; Hiley, C.I.; Sharman, J.D.B.; Wells, P.P.; Russell, A.E.; Kashtiban, R.J.; Sloan, J.; Walton, R.I. Water-splitting electrocatalysis in acid conditions using ruthenate-iridate pyrochlores. *Angew. Chem. Int. Ed. Engl.* **2014**, *53*, 10960–10964. [[CrossRef](#)]
4. Li, Y.; Hasin, P.; Wu, Y. Ni_xCo_{3-x}O₄ Nanowire Arrays for Electrocatalytic Oxygen Evolution. *Adv. Mater.* **2010**, *22*, 1926–1929. [[CrossRef](#)] [[PubMed](#)]
5. Dionigi, F.; Strasser, P. NiFe-Based (Oxy)hydroxide Catalysts for Oxygen Evolution Reaction in Non-Acidic Electrolytes. *Adv. Energy Mater.* **2016**, *6*, 1600621. [[CrossRef](#)]
6. Osgood, H.; Devaguptapu, S.V.; Xu, H.; Cho, J.; Wu, G. Transition metal (Fe, Co, Ni, and Mn) oxides for oxygen reduction and evolution bifunctional catalysts in alkaline media. *Nano Today* **2016**, *11*, 601–625. [[CrossRef](#)]
7. Castro, E.B.; Real, S.G.; Pinheiro Dick, L.F. Electrochemical characterization of porous nickel–cobalt oxide electrodes. *Int. J. Hydrogen Energy* **2004**, *29*, 255–261. [[CrossRef](#)]
8. Chi, B.; Lin, H.; Li, J.; Wang, N.; Yang, J. Comparison of three preparation methods of NiCo₂O₄ electrodes. *Int. J. Hydrogen Energy* **2006**, *31*, 1210–1214. [[CrossRef](#)]

9. Fan, G.; Li, F.; Evans, D.G.; Duan, X. Catalytic applications of layered double hydroxides: Recent advances and perspectives. *Chem. Soc. Rev.* **2014**, *43*, 7040–7066. [[CrossRef](#)]
10. Cheng, F.; Shen, J.; Peng, B.; Pan, Y.; Tao, Z.; Chen, J. Rapid room-temperature synthesis of nanocrystalline spinels as oxygen reduction and evolution electrocatalysts. *Nat. Chem.* **2011**, *3*, 79–84. [[CrossRef](#)]
11. Bragg, W.H. The Structure of Magnetite and the Spinels. *Nature* **1915**, *95*, 561. [[CrossRef](#)]
12. Liu, X.-M.; Cui, X.; Dastafkan, K.; Wang, H.-F.; Tang, C.; Zhao, C.; Chen, A.; He, C.; Han, M.; Zhang, Q. Recent advances in spinel-type electrocatalysts for bifunctional oxygen reduction and oxygen evolution reactions. *J. Energy Chem.* **2021**, *53*, 290–302. [[CrossRef](#)]
13. Wang, J.; Qiu, T.; Chen, X.; Lu, Y.; Yang, W. Hierarchical hollow urchin-like NiCo₂O₄ nanomaterial as electrocatalyst for oxygen evolution reaction in alkaline medium. *J. Power Source* **2014**, *268*, 341–348. [[CrossRef](#)]
14. Xia, H.; Huang, Z.; Lv, C.; Zhang, C. A Self-Supported Porous Hierarchical Core–Shell Nanostructure of Cobalt Oxide for Efficient Oxygen Evolution Reaction. *ACS Catal.* **2017**, *7*, 8205–8213. [[CrossRef](#)]
15. Bandal, H.A.; Jadhav, A.R.; Tamboli, A.H.; Kim, H. Bimetallic iron cobalt oxide self-supported on Ni-Foam: An efficient bifunctional electrocatalyst for oxygen and hydrogen evolution reaction. *Electrochim. Acta* **2017**, *249*, 253–262. [[CrossRef](#)]
16. Doyle, R.L.; Godwin, I.J.; Brandon, M.P.; Lyons, M.E.G. Redox and electrochemical water splitting catalytic properties of hydrated metal oxide modified electrodes. *Phys. Chem. Chem. Phys.* **2013**, *15*, 13737–13783. [[CrossRef](#)]
17. Shinagawa, T.; Garcia-Esparza, A.T.; Takahashi, K. Insight on Tafel slopes from a microkinetic analysis of aqueous electrocatalysis for energy conversion. *Sci. Rep.* **2015**, *5*, 13801. [[CrossRef](#)]
18. Park, G.; Shin, C.-H.; Kang, J.; Lee, K.-S.; Zhang, C.; Lim, B.; Kim, C.; Yu, J.-S. Controllable synthesis of single-layer graphene over cobalt nanoparticles and insight into active sites for efficient oxygen evolution. *J. Mater. Chem. A* **2021**, *9*, 12060–12073. [[CrossRef](#)]
19. Suen, N.-T.; Hung, S.-F.; Quan, Q.; Zhang, N.; Xu, Y.-J.; Chen, H.M. Electrocatalysis for the oxygen evolution reaction: Recent development and future perspectives. *Chem. Soc. Rev.* **2017**, *46*, 337–365. [[CrossRef](#)]
20. Hu, J.; Zhang, C.; Meng, X.; Lin, H.; Hu, C.; Long, X.; Yang, S. Hydrogen evolution electrocatalysis with binary-nonmetal transition metal compounds. *J. Mater. Chem. A* **2017**, *5*, 5995–6012. [[CrossRef](#)]
21. Chen, K.; Rajendiran, R.; Lee, D.H.; Diao, J.; Li, O.L. Core-double shells heterostructure γ -Fe₂O₃@FeS₂@C nanocubics with energy level matching double interfaces to boost the oxygen evolution reaction. *J. Alloys Compd.* **2021**, *885*, 160986. [[CrossRef](#)]
22. Buchner, F.; Fuchs, S.; Behm, R.J. UHV preparation and electrochemical/-catalytic properties of well-defined Co- and Fe-containing unary and binary oxide model cathodes for the oxygen reduction and oxygen evolution reaction in Zn-air batteries. *J. Electroanal. Chem.* **2021**, *896*, 115497. [[CrossRef](#)]
23. Ma, S.; Sun, L.; Cong, L.; Gao, X.; Yao, C.; Guo, X.; Tai, L.; Mei, P.; Zeng, Y.; Xie, H.; et al. Multiporous MnCo₂O₄ Microspheres as an Efficient Bifunctional Catalyst for Nonaqueous Li–O₂ Batteries. *J. Phys. Chem. C* **2013**, *117*, 25890–25897. [[CrossRef](#)]
24. Liu, L.; Yang, Y. Shape-controlled synthesis of MnCo complex oxide nanostructures via a polyol-based precursor route and their catalytic properties. *Superlattices Microstruct.* **2013**, *54*, 26–38. [[CrossRef](#)]
25. Zhang, H.; Chen, B.; Jiang, H.; Duan, X.; Zhu, Y.; Li, C. Boosting water oxidation electrocatalysts with surface engineered amorphous cobalt hydroxide nanoflakes. *Nanoscale* **2018**, *10*, 12991–12996. [[CrossRef](#)]
26. Guzmán-Vargas, A.; Vazquez-Samperio, J.; Oliver-Tolentino, M.A.; Nava, N.; Castillo, N.; Macías-Hernández, M.J.; Reguera, E. Influence of cobalt on electrocatalytic water splitting in NiCoFe layered double hydroxides. *J. Mater. Sci.* **2018**, *53*, 4515–4526. [[CrossRef](#)]
27. Thommes, M. Physical Adsorption Characterization of Nanoporous Materials. *Chem. Ing. Tech.* **2010**, *82*, 1059–1073. [[CrossRef](#)]
28. Wei, X.; Li, Y.; Peng, H.; Gao, D.; Ou, Y.; Yang, Y.; Hu, J.; Zhang, Y.; Xiao, P. A novel functional material of Co₃O₄/Fe₂O₃ nanocubes derived from a MOF precursor for high-performance electrochemical energy storage and conversion application. *Chem. Eng. J.* **2019**, *355*, 336–340. [[CrossRef](#)]
29. Samanta, A.; Das, S.; Jana, S. Doping of Ni in α -Fe₂O₃ Nanoclews To Boost Oxygen Evolution Electrocatalysis. *ACS Sustain. Chem. Eng.* **2019**, *7*, 12117–12124. [[CrossRef](#)]
30. Zhu, S.; Huang, L.-A.; He, Z.; Wang, K.; Guo, J.; Pei, S.-E.; Shao, H.; Wang, J. Investigation of oxygen vacancies in Fe₂O₃/CoO_x composite films for boosting electrocatalytic oxygen evolution performance stably. *J. Electroanal. Chem.* **2018**, *827*, 42–50. [[CrossRef](#)]
31. Yang, X.; Chen, J.; Chen, Y.; Feng, P.; Lai, H.; Li, J.; Luo, X. Novel Co₃O₄ Nanoparticles/Nitrogen-Doped Carbon Composites with Extraordinary Catalytic Activity for Oxygen Evolution Reaction (OER). *Nano-Micro Lett.* **2017**, *10*, 15. [[CrossRef](#)]
32. Pei, Z.; Xu, L.; Xu, W. Hierarchical honeycomb-like Co₃O₄ pores coating on CoMoO₄ nanosheets as bifunctional efficient electrocatalysts for overall water splitting. *Appl. Surf. Sci.* **2018**, *433*, 256–263. [[CrossRef](#)]
33. Li, D.; Park, E.J.; Zhu, W.; Shi, Q.; Zhou, Y.; Tian, H.; Lin, Y.; Serov, A.; Zulevi, B.; Baca, E.D.; et al. Highly quaternized polystyrene ionomers for high performance anion exchange membrane water electrolyzers. *Nat. Energy* **2020**, *5*, 378–385. [[CrossRef](#)]
34. Xiao, J.; Oliveira, A.M.; Wang, L.; Zhao, Y.; Wang, T.; Wang, J.; Setzler, B.P.; Yan, Y. Water-Fed Hydroxide Exchange Membrane Electrolyzer Enabled by a Fluoride-Incorporated Nickel–Iron Oxyhydroxide Oxygen Evolution Electrode. *ACS Catal.* **2021**, *11*, 264–270. [[CrossRef](#)]
35. Zha, Q.; Li, M.; Liu, Z.; Ni, Y. Hierarchical Co,Fe-MOF-74/Co/Carbon Cloth Hybrid Electrode: Simple Construction and Enhanced Catalytic Performance in Full Water Splitting. *ACS Sustain. Chem. Eng.* **2020**, *8*, 12025–12035. [[CrossRef](#)]

36. Li, M.; Liu, T.; Bo, X.; Zhou, M.; Guo, L. A novel flower-like architecture of FeCo@NC-functionalized ultra-thin carbon nanosheets as a highly efficient 3D bifunctional electrocatalyst for full water splitting. *J. Mater. Chem. A* **2017**, *5*, 5413–5425. [[CrossRef](#)]
37. Shin, C.-H.; Wei, Y.; Park, G.; Kang, J.; Yu, J.-S. High performance binder-free Fe–Ni hydroxides on nickel foam prepared in piranha solution for the oxygen evolution reaction. *Sustain. Energy Fuels* **2020**, *4*, 6311–6320. [[CrossRef](#)]
38. Jang, M.J.; Yang, J.; Lee, J.; Park, Y.S.; Jeong, J.; Park, S.M.; Jeong, J.-Y.; Yin, Y.; Seo, M.-H.; Choi, S.M.; et al. Superior performance and stability of anion exchange membrane water electrolysis: pH-controlled copper cobalt oxide nanoparticles for the oxygen evolution reaction. *J. Mater. Chem. A* **2020**, *8*, 4290–4299. [[CrossRef](#)]